Smart Toolkit for Fluorescence Tomography: Simulation, Reconstruction, and Validation

Wuwei Ren, Helene Isler, Martin Wolf, Jorge Ripoll, and Markus Rudin

Abstract—*Objective:* Fluorescence molecular tomography (FMT) can provide valuable molecular information by mapping the bio-distribution of fluorescent reporter molecules in the intact organism. Various prototype FMT systems have been introduced during the past decade. However, none of them has evolved as a standard tool for routine biomedical research. The goal of this paper is to develop a software package that can automate the complete FMT reconstruction procedure. *Methods:* We present smart toolkit for fluorescence tomography (STIFT), a comprehensive platform comprising three major protocols: 1) virtual FMT, i.e., forward modeling and reconstruction of simulated data; 2) control of actual FMT data acquisition; and 3) reconstruction of experimental FMT data. *Results:* Both simulation and phantom experiments have shown robust reconstruction results for homogeneous and heterogeneous tissue-mimicking phantoms containing fluorescent inclusions. *Conclusion:* STIFT can be used for optimization of FMT experiments, in particular for optimizing illumination patterns. *Significance:* This paper facilitates FMT experiments by bridging the gaps between simulation, actual experiments, and data reconstruction.

Index Terms—Fluorescence tomography, finite element modeling, image reconstruction, optimization, validation.

I. INTRODUCTION

FLUORESCENCE molecular tomography (FMT) has become an attractive technology for biomedical research with its ability to map the distribution of fluorescent reporter molecules thereby providing 3D information on molecular processes in the intact organism [1]–[3]. In a typical FMT experiment, a point light source is scanned across the sample and the

light distribution on the sample surface both at the excitation and fluorescence wavelength is recorded. Collecting data from a sufficient number of source positions allows three-dimensional reconstruction of the fluorophore distribution within the sample. A variety of FMT prototypes have been proposed involving different illumination and detection schemes [4]–[6], time-dependent or -independent measurements [7]–[9], as well as various reconstruction algorithms [10]–[14]. [3] is a good review for various implementations of FMT. Despite the availability of commercial scanners, most FMT systems currently in use are home-built. Hence, there is no standardization or robust validation. Correspondingly, FMT cannot yet be seen as an established technology for biomedical research. Reasons preventing FMT from becoming a workhorse include lengthy measurement time due to the sequential nature of data acquisition, the lack of standardized and validated procedures for experimental design, data acquisition and image reconstruction, and the absence of proper validation and quality control e.g., using standardized tissue phantoms.

Data acquisition in FMT is an interactive procedure: the user has to define an illumination pattern on the sample surface. Although strategies for optimizing the illumination pattern exist [4], [15]–[17], none of them can be considered as accepted standard. Data reconstruction is based on sophisticated forward modelling and inversion methods. Proper selection of reconstruction strategy requires expert knowledge. Verification of reconstruction methods remains an issue as there are no standardized tools available for calibration such as tissue mimicking phantoms. Moreover, data acquisition, image reconstruction and validation are interlinked; for example the measurement configuration may impact the choice of reconstruction methods. A trade-off between measurement/computational time and reconstruction accuracy has to be found. Finally, a user-friendly software platform is required for the deployment of FMT.

With regard to the light propagation model applied, software solutions for diffuse optical tomography (DOT) and FMT can be classified into two major categories: finite-element-method (FEM)-based and Monte-Carlo (MC)-based methods. In FEM-based methods, the object is discretized into a 2D or 3D finite mesh and the diffusion equation (DE), a second order partial differential equation, is solved for each nodal point. Considering the computational expense, FEM is still the most commonly used algorithm for treating DOT and FMT problems with NIRFast [18] and Toast++ [19], [20] being the most established tools. Both software packages can handle heterogeneous optical properties inside the object, irregular air/tissue boundaries,

multispectral data, and different modes of operation (frequency/time domain). Regarding inversion, both NIRFast and Toast++ provide a range of regularized approaches. Toast++ focuses on computational efficiency and modular design of the software suites. It integrates C++ libraries for sparse matrix algebra, finite-element analysis and nonlinear inverse problem solver and facilitates rapid prototyping via script-based programming languages like MATLAB (MathWorks, US) and PYTHON. On the other hand, NIRFast offers a comprehensive platform for treating general optical tomographic problems. A segmentation and meshing toolbox was developed for handling multimodal images [20]. A recent version of NIRFast can visualize the reconstructed data in 3D by linking NIRFast to the open-source software Slicer [21]. In addition to these freeware packages, commercial general-purposed FEM-based software tools such as COMSOL (COMSOL Inc., US) have been used in FMT [22]. A critical prerequisite for FEM-based simulation is proper meshing of the object. Hence, multiple meshing toolboxes have been applied, including GMSH [23], iso2mesh [14], and COMSOL [24].

While FEM-based software tools use an ensemble equation to describe photon propagation in the medium, the MC-based methods estimate the photon distribution after launching a large number of independent random trials. MC simulation solves the radiative transfer equation without the need for simplification as implied by DE. Consequently it generates more accurate results than FEM in heterogeneous media, especially when the media comprise low-scattering regions. Inspired by some classic simulators such as MCML [25], modern MC-based software capitalizes on parallel computation techniques with low-cost graphic cards, which massively increased computational speed [26]. Main features of the four most popular MC-based software platforms (MCX, MOSE, MMC, TIM-OS) are listed in Table I. Despite the increasing popularity of MC-based software tools [27], it is still considered a computationally expensive method. In addition, none of the previously reported MC-based software packages provides inversion functions like NIRFast and Toast++.

Apart from software tools provided with commercial systems, there is currently no single software package that could handle the whole FMT procedure from acquisition control to data reconstruction. The software packages discussed above are focused on image reconstruction and do not comprise data acquisition modules. Typically, the acquisition module is a part of hardware development and based on fast prototyping tools like LabVIEW [2], [3]. There is no immediate link between measurement and reconstruction algorithm in most cases. A seamless integration of reconstruction and measurement would allow generating virtual FMT prior to a real data acquisition, thereby enabling the optimization of experimental protocols.

Here, we present Smart Toolkit for Fluorescence Tomography (STIFT), a software solution framing the whole FMT procedure. STIFT includes five modules: i) a tool for optimizing the design of the FMT experiment (a simulator), ii) a data acquisition tool based on the optimal design (a controller), iii) a module for robust 3D reconstruction (a reconstructor), iv) a quality control feature (a viewer), and v) a setting and feedback module for iterative adjustments (a configurator).

Virtual FMT protocol can test the feasibility of a specific FMT measurement and generate the optimal experimental design, i.e., define an optimized illumination pattern. This optimized pattern will then be used for the experimental FMT protocol. Performance evaluation of STIFT included studies with phantoms of different levels of complexity and with a animal disease model, yielding robust reconstruction results.

II. METHODS

A. Theoretical Background

Light propagation in turbid media can be approximated by the DE [18]. In the frequency domain, the DE can be expressed as:

$$-\nabla \cdot \kappa(r)\nabla\phi(r,\omega) + \left[\mu_a(r) + \frac{i\omega}{c}\right]\phi(r,\omega) = 0, \quad r \in \Omega \tag{1}$$

where the absorption coefficient $\mu_a(r)$ and the diffusion coefficient $\kappa(r)$ depend on the location r within the object domain Ω. The field $\phi(r,\omega)$ denotes the photon density distribution, c the speed of light in the medium and ω the modulation frequency. At tissue interfaces (e.g., when considering non-contact FMT) we have to use a Robin type boundary condition,

$$\phi(m,w) + 2\zeta(c)\kappa(m)\frac{\partial\phi(m,\omega)}{\partial v} = q(m,\omega), \quad m \in \partial\Omega \tag{2}$$

with a term $\zeta(c)$ addressing the refractive index mismatch and $q(m,\omega)$ accounting for the source term at the boundary domain $\partial\Omega$. ∂v denotes the outward normal at the surface. In the following, we are dealing with continuous-wave (CW) mode FMT, hence ω can be set to 0.

In the FEM formalism, the Galerkins method [18] simplifies the DE to a linear equation, $S\Phi = Q$, with S denoting the system matrix, Φ a vector comprising the nodal value of field ϕ, and Q a vector comprising the nodal source term. For a standard FMT measurement composed of excitation and emission procedures, the resulted coupled DEs may hence be written as:

$$S_x\Phi_{x,i} = Q_{x,i}, \quad i = 1, 2 \cdots n_l \tag{3}$$

$$S_m\Phi_{m,i} = Q_{m,i}, \quad i = 1, 2 \cdots n_l \tag{4}$$

The subscripts x and m stand for the excitation and emission procedures respectively, while i indicates the source number. During the excitation, source term $Q_{x,i}$ is determined by the laser profile L_i, while for the emission, $Q_{m,i} = \eta \cdot diag(C_d)\Phi_{x,i}$, where C_d is the vector containing the nodal values of fluorescence concentration and η the fluorescence quantum yield. The operation $diag(C_d)$ converts the column vector C_d into a diagonal matrix.

To more accurately predict the signal M received by detectors at the excitation and emission wavelength, a transportation matrix Γ is introduced to describe free-space light propagation from the object surface to the virtual detector plane

$$M_x = \Gamma^T \Phi_x \tag{5}$$

$$M_m = \Gamma^T \Phi_m \tag{6}$$

TABLE I
COMPARISON OF STIFT AND OTHER AVAILABLE SOFTWARES

Features	NIRFast	Toast++	MMC	MCX	TIM-OS	MOSE	STIFT
Data acquisition	N	N	N	N	N	N	Y
Forward model	FEM	FEM	mesh-baed MC	voxel-based MC	mesh-baed MC	mesh-based MC	FEM
Light modulation	FD/CW	TD/FD/CW	TD/FD/CW	TD/FD/CW	TD/FD/CW	TD/FD/CW	FD/CW
Meshing	Y	N	N	N	N	N	Y
Generation of optical properties	N	N	N	N	N	N	Y
Registration	N	N	N	N	N	N	Y
Reconstruction	Y	Y	N	N	N	N	Y
Visualization	Y	Y	Y	Y	N	Y	Y
Application	DOT/BLT/FMT	DOT/BLT/FMT	DOT/BLT/FMT	DOT/BLT/FMT	DOT/BLT/FMT	DOT/BLT/FMT	FMT
GUI	Y	N	N	N	N	Y	N

[1]Comparison of STIFT and other available softwares regarding their basic features including data acquisition, forward model, light modulation, segmentation/meshing tool, generation of optical properties, image registration, reconstruction visualization, application, and graphic user interface (GUI). STIFT is an FEM-based software focusing on FMT, whereas other software tools have more general application on DOT, FMT, and Bioluminance tomography (BLT).

Γ incorporates a visibility term describing whether a surface element is visible from a detector element, the numerical aperture of lens, the distance from the surface to the detector, the area of a surface element and the geometry of object surface [28]. Detailed explanations can be found in the supplementary material. The normalized value $Y = M_m/M_x$, given as the ratio between M_m, the emission measurement and M_x, the corresponding excitation measurement, is used for the final reconstruction [29].

To control the reconstruction accuracy and ease the data fusion with data derived from another modality, we introduce a mapping matrix T_c to link C_d in the context of a tetrahedral mesh to C_{recon} referring to a Cartesian grid.

$$C_d = T_c^T C_{recon} \tag{7}$$

Finally, Y can be expressed by the product of the weighting matrix, W times the unknown variable vector, C_{recon}.

$$Y = WC_{recon} \tag{8}$$

where $W = W_d T_c^T$ with the elements $W_d(h, n)$

$$W_d(h,n) = \frac{\eta \Gamma_k^T gm_n \Phi_{x,i}(n)}{\Gamma_k^T \Phi_{x,i}} \tag{9}$$

$$h = n_m(i-1) + k \text{ and } n = 1, 2, \ldots, n_d$$

n_m is the number of pixels on the detector plane, and n_d the number of the unknowns. gm_i are the column vectors of the S_m^{-1}, introduced in (4).

$$S_m^{-1} = \begin{bmatrix} gm_1 & gm_2 & \cdots & gm_{n_d} \end{bmatrix} \tag{10}$$

The recovery of the fluorescence concentration C_{recon} is implemented by minimizing a cost function $\Psi(C_{recon})$ upon addition of a regularization term $\lambda\|C_{recon}\|^2$ and non-negativity constraints ($C_{recon} \geq 0$) using limited-memory BFGS algorithm, a quasi-Newton method [30], [31].

$$\Psi(C_{recon}) = \frac{1}{2}\|WC_{recon} - \tilde{Y}\|^2 + \lambda\|C_{recon}\|^2 \tag{11}$$

Here $\tilde{Y}$ denotes the measured normalized value.

B. The Framework of STIFT

STIFT is based on object-oriented MATLAB programming using several MATLAB classes/packages including a home-built class using the same name (STIFT), a forward modelling/reconstruction suite (Toast++) [18], a meshing manipulation package (iso2mesh) [32], and an inverse problem solver (AIR toolbox) [24]. The STIFT class plays a pivotal role in organizing and linking the individual classes or packages to form a framework providing an optimized FMT experimental protocol. Input parameters of STIFT contain physical parameters defining the problem (optical properties, laser, detector, noise) and modelling parameters for the reconstruction (meshing, regularization). Output values include the weighting matrix and local fluorescence dye concentration. The detailed list of STIFT properties and methods is compiled in the supplementary material. The STIFT software package uses the concept of state machines: instead of giving a rigid workflow for all different studies, STIFT allows users to select different protocols and define an optimized setting for the measurement and reconstruction. STIFT comprises five modules: configurator, simulator, controller, reconstructor, and viewer. These five modules contain several functional methods that are combined into three protocols (Fig. 1):

a) Virtual FMT: configurator ⇒ simulator ⇒ reconstructor ⇒ viewer
b) Experimental setup and data acquisition: configurator ⇒ controller ⇒ (experimental data)
c) Reconstruction of experimental data: configurator (experimental data) ⇒ reconstructor ⇒ viewer

C. Features of STIFT

Four essential features of STIFT are described including 1) self-adaptive meshing, 2) image registration, 3) free-space detection, and 4) mapping technique.

1) Self-Adaptive Meshing: Although Toast++ is capable of rapid forward modelling using its unique library for sparse matrix operation (libmath) [18], there is no function to transfer a voxelized image set into a readable mesh within Toast++.
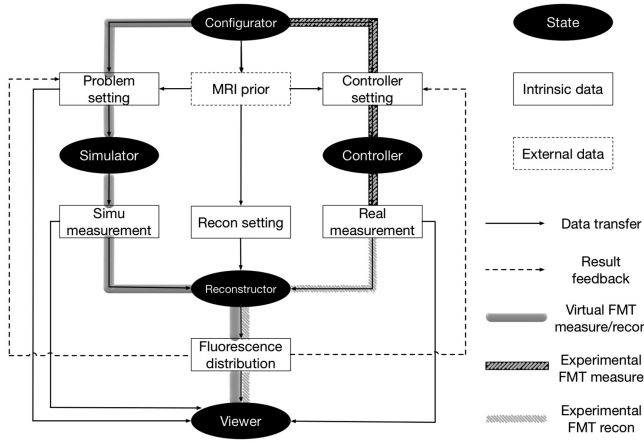
Fig. 1. Schematic of STIFT. The dark ellipsoids indicate the five modules of STIFT, including configurator, simulator, controller, reconstructor, and viewer. The squares with solid and dashed boundaries denote intrinsic and external data respectively. Three protocols are indicated with thick lines: 1) virtual FMT (thick gray line), 2) real FMT measurement (black hatched line), and 3) experimental FMT reconstruction (hatched gray line). Data transfer is displayed with solid thin line whereas the result feedback is shown in dashed thin lines.
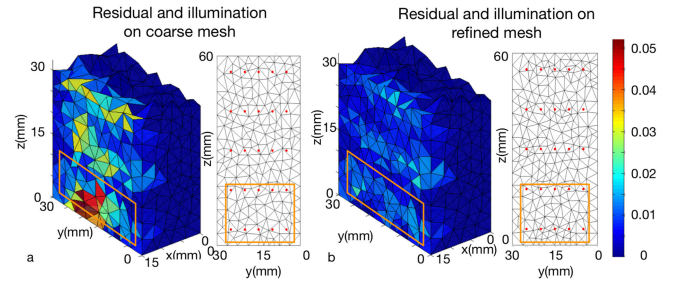

Fig. 2. Illumination-adaptive mesh refinement. The colored tetrahedral elements on left side of each image indicate the residual or relative errors for FEM. (a) Elements with large errors (the region indicated by the orange box) will be broken up to several sub-elements, resulting in smaller residuals. (b) The red dots indicate source locations.

GMSH [23] is recommended as a convenient external software for qualified meshing, but the interactive user interface of GMSH could only provide meshes for a limited number of regular-shaped geometries. Here, we applied an open-source meshing toolbox, iso2mesh [32], capable of delivering meshing for complicated geometries and irregular curved surfaces. While the accuracy of FEM can be improved by using small elements, there is always a trade-off between accuracy and computational cost. Adaptive meshing is used to remedy this problem. First, a binary image dataset from the structural reference data (typically derived from CT or MRI) is generated. Second, the binary image is plugged into iso2mesh to generate a coarse mesh. Finally, the coarse mesh is further refined by using:

1) Geometry-adaptive refinement: A Laplacian operator is applied to the voxelized image stack to identify the edges of inner structures. The edge map in the grid is then mapped to the coarse mesh. Each element mapped with a binary edge signal is then split into finer elements (More details in supplementary material).

2) Illumination-adaptive refinement: The laser sources are first assigned to the surface of the coarse mesh. Forward modelling of the excitation procedure is then carried out on the coarse mesh. The residual for each element is then calculated based on the DE. The elements with higher residual values are broken up into more sub-elements than those with lower residual values. The number of sub-elements that one element generates is inversely proportional to the residuals. Fig. 2(a) and (b) compare the residual values of coarse and refined meshes. There is a trend that elements close to the illumination sources are more likely to break into more sub-elements.

2) Image Registration: STIFT provides a simple landmark-based registration function to fuse the structural

reference with functional image. For slab phantoms, the landmarks are normally selected at corners, whereas for mice the landmarks are selected as clearly identifiable anatomical structures such as eyes, ears or nose tip, landmarks that can be easily identified on both the white-light image and the topological MRI map (More details in supplementary material).

3) Free-Space Detection: A non-contact configuration of FMT reduces complexity of instrumentation and eases the experimental manipulation. In this case, in addition to describing photon propagation within the biological tissue, the model has to account for free-space photon propagation between the sample surface and the detector. This is achieved by projecting the individual elements of the CCD sensor to a virtual imaging plane (focal plane). All the normals of virtual pixels were calculated. The outward optical flux obeys Lamberts cosine law [28], [33] (More details in supplementary material).

4) Mapping Technique: As the prior information is derived from a structural imaging modality (e.g., MRI) with data typically given in Cartesian ordinates, it is necessary to relate it to the optimized mesh for FMT modelling and reconstruction. For the convenience of data fusion and result analysis, the FMT reconstruction results are transformed from the mesh-based nodal format into a Cartesian grid. The final weighting matrix W in (8) contains the mapping matrix T_c defined in (7) such that the number of unknowns can be adjusted. STIFT uses linear interpolation to transform the detector plane, the assignment of optical parameters, and the distribution of fluorescence dye from the optimized mesh into the Cartesian grid coordinates.

D. Validation Based on Silicone Phantoms

To validate the performance of STIFT, three optical phantoms of increasing complexity (Fig. 3) have been used. Information regarding phantom design, dimension, optical properties, fabrication and calibration is given in the supplementary material. The virtual FMT protocol was used to design the illumination patterns for each phantom. The actual experiment was then carried out using the optimized design of illumination, followed by image reconstruction. Statistical post-processing was performed to objectively compare reconstructed results with the ground truth.
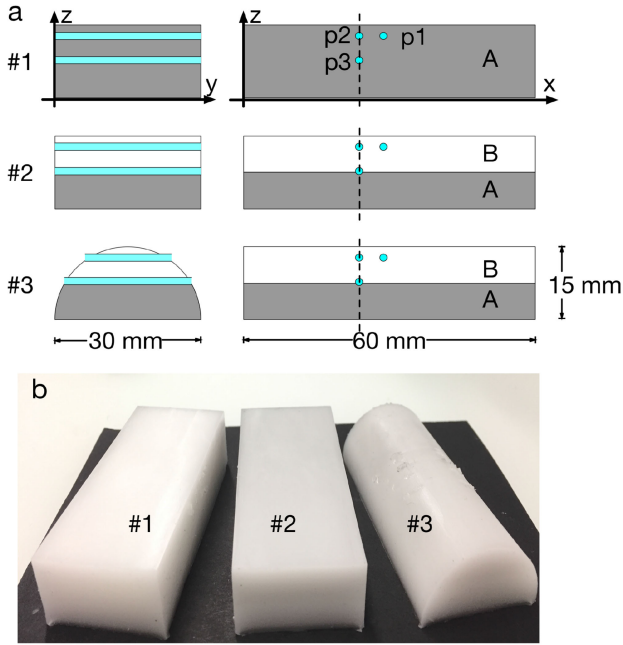
Fig. 3. Phantoms for validation purpose. (a) Structure and dimension of each phantom. Labels p1, p2, and p3 indicate holes (light blue) located at the same positions for all phantoms: p1 and p2 are both 3-mm below the surface and separated by 5 mm (center-to-center), whereas p2 and p3 are aligned in the same vertical plane p3 being 7 mm from the surface. All three holes have a diameter of 1.5 mm for placing one 1-mm-diameter glass capillary. (b) Photograph of fabricated phantoms. (Optical properties of component A and B consisting these phantoms are described in supplementary material).

1) Validation of Virtual FMT Function:

Carrying out a virtual FMT protocol allows examining the feasibility of actual FMT experiments and optimizing the experimental design. This is illustrated for the homogeneous phantom #1 containing inclusions in p1 and p2, for which virtual FMT was used to optimize the illumination pattern, a key setting for the FMT experiment.

Configuration of the problem constitutes the first step in the modelling process. The object was defined as slab phantom with the size of 60 mm × 30 mm × 15 mm and homogeneous optical properties, i.e., an absorption coefficient μ_a of 0.007 mm^{-1} and a scattering coefficient μ_s of 0.87 mm^{-1}. The virtual detector array comprised 60 × 30 elements. The area of individual detector elements was 1 mm × 1 mm, i.e., the detection array covered the whole surface (x, y-plane) of the phantom. The measurement was performed in the reflection mode, indicating that the images were recorded from the same side as the illumination. The Cartesian grid for assigning reconstruction values had the dimension of 36 × 18 × 9. White noise of an amplitude of 1% of the overall mean intensity was added.

To accurately describe the illumination pattern, we introduced three parameters: i) the lateral number of illumination points N_{illu}, ii) the lateral length l_{SF} of scanning field (SF), and iii) the illumination density δ indicating the number of illumination points per millimeter and given by (12). All of the illumination patterns were square-shaped, consisted of a $N_{illu} \times N_{illu}$ grid of point sources, covering an area of $l_{SF} \times l_{SF}$ (Fig. 4(b)).

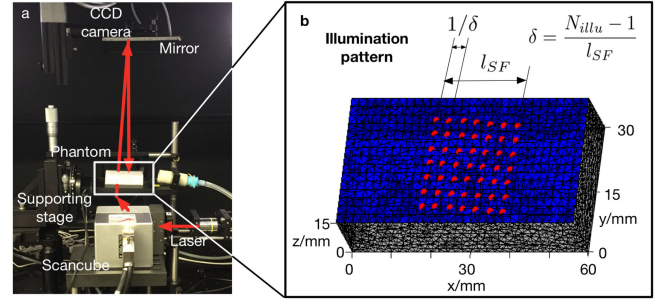$$\delta = \frac{N_{illu} - 1}{l_{SF}} \quad (12)$$

Fig. 4. (a) FMT system and its experimental setup indicating the positions of CCD camera, supporting stage, Scancube, laser source and the loaded phantom. The read arrow shows the optical path to the phantom surface in reflection mode. (b) The simulated object for phantom #1 with a laser excitation grid (red spots) and detection arrays (60 × 30) covering the whole surface of x, y-plane (blue patches). The illumination patterns were square-shaped, consisted of a $N_{illu} \times N_{illu}$ grid of point sources, here $N_{illu} = 7$.

Multiple illumination patterns were simulated for optimization purpose. We assumed that the minimum step for steering laser beams is d (here $d = 2.307 +/- 0.001$ mm). Each SF was centered at the midpoint of the phantom located above the inclusion in p1 and l_{SF} was given by $n \cdot d$ ($n = 1, 2, \ldots, 10$). For a given l_{SF}, different illumination density parameters were tested with $N_{illu} = 2, 3, \ldots, (n + 1)$. For each illumination pattern, the concentration of fluorescent dye was reconstructed using the reconstruction module of STIFT. Reconstruction results were visualized for several illumination patterns (for a fixed illumination density, $\delta = 1/d$, $N_{illu} = 2, 5, 8, 10$). Root-mean-square error (RMSE) [34] were calculated to evaluate the reconstruction quality for each illumination pattern. The setting, which generates the minimal value of RMSE, is considered as the optimal design for the experimental FMT.

2) Validation of Experimental FMT Function:

Following virtual FMT simulations, experiments have been carried out using the three phantoms and a previously described homebuilt FMT system [6]. The system includes a 16-bit CCD camera (ANDOR Corporation, Belfast, Northern Ireland) with 1024 × 1024 pixels for detection, a galvanometric driven mirror system (Scancube, ScanLab, Puchheim, Germany) for steering the laser beam, a solid-state laser generator with 670 nm wavelength for illumination (B&W Tek, Newark, USA), and a custom-made sample support (Fig. 4(a)) [6]. The fluorescence source consisted of a 1 mm diameter capillary filled with a drop of cyanine5.5 (Cy5.5) with a concentration of 2 nmol/ml. The wavelength of filters for excitation and emission procedures were set to 680 nm and 700 nm respectively, which could be easily adjusted with the filter wheel integrated in the FMT system.

The purpose of the experimental part of FMT was i) to validate the result of virtual FMT optimization procedure and ii) to assess the accuracy of FMT reconstruction for different complexity of object.

For validating the optimization result, we used the fixed δ of $1/d$ and N_{illu} values ranging from 2 to 11, or l_{SF} from 2.3 mm to 23.1 mm. The settings for phantom geometry, optical properties, detector array, and reconstruction grid remain identical to the virtual FMT part. For each illumination pattern,

the fluorescence signal was reconstructed and the RMSE calculated with regard to the dye distribution on the basis of the phantom geometry. Finally, RMSE values from virtual and experimental FMT protocols were compared to validate the results of the optimization procedure.

Identical Cy5.5-filled capillaries were inserted into p1 position in all three phantoms (Fig. 3). FMT experiments were carried out both in reflection and transmission mode for the three phantoms, resulting in six sets of reconstruction data. For the reflection mode, a 7×7 illumination pattern was used covering an area of 14 mm $\times$ 14 mm, whereas for the transmission mode experiments, a 5×5 grid covering an area 15 mm $\times$ 15 mm was selected. The scanning area for transmission mode is smaller than the reflection one because of the limited dimension of the window embedded in the animal support. For the same phantom, the measurements with reflection and transmission modes were performed sequentially, without moving the phantom. A reconstruction grid of $41 \times 21 \times 11$ was applied for all phantoms. Contrast to noise ratio (CNR) [35] and RMSE were calculated to assess the reconstruction performance for each case.

E. In Vivo Application With a Tumor Animal Model

1) Animal Preparation: A female BALB/c-nu mouse (7 weeks of age; bodyweight: 20 g) was used as a tumor model to test the reconstruction performance of STIFT. 4T1 breast cancer cells were cultured and injected subcutaneously in the left flank with 10^6 cells in 100 μL phosphate-buffered saline (PBS) [36]. All experiments were performed in accordance with the Swiss Federal Act on Animal Protection and were approved by the Cantonal Veterinary Office Zurich (Permit Number: 18-2014). All procedures fulfil the ARRIVE guidelines on reporting animal experiments.

2) Data Acquisition With FMT and MRI: ProSense 680 (Perkin Elmer, MA, USA; ProSense for short in the text that follows) was used to asses protease activity in the tumor model. The probe becomes highly fluorescent following protease-mediated activation [37]. Excitation and emission wavelengths for ProSense are 680 nm and 700 nm respectively. ProSense was administrated 24 hours prior to the imaging experiment using the recommended dose of 2 nmol/150 μL in PBS buffer. Prior to the fluorescence measurement a white-light image was recorded. Then an illumination grid of 8×10 laser point sources was defined covering an area of 14×18 mm^2 on the left flank. For each illumination point, both an excitation and emission map has been recorded. The wavelength of the bandpass filter was set to 660 $+/-13$ nm for the excitation, and 700 $+/-13$ nm for the emission measurement according to the spectrum of ProSense [38].

To obtain anatomical reference used for meshing and assigning optical properties, we imaged the same mouse with a fixed support using MRI. The experiment was carried out using a BioSpec 94/30 scanner (Bruker BioSpin GmbH, Ettlingen, Germany) equipped with a 9.4 T magnet, 30 cm clear bore, a high performance B-GA 12S gradient system, and a phased-array mouse brain CryoProbe for signal reception in combination with a whole body birdcage resonator for radiofrequency (RF) transmission. Multislice T2*-weighted MR images were recorded using a gradient echo sequence with the following parameters: field-of-view (FOV) = 40×40 mm^2, number of slices = 35, dimension of reconstructed matrix = $256 \times 256 \times 35$, slice thickness = 0.7 mm, repetition delay (TR) = 1500 ms, echo delay (TE) = 8.102 ms, and pulse angle α = 90 degree.

3) Reconstruction and Validation: We used the reconstructor module of STIFT to recover the three-dimensional distribution of injected ProSense. Firstly, the T2*-weighted MR images were loaded for meshing and the white-light image was registered to the topological MRI map, which represents the mouse surface, using a natural landmark-based registration method. Then absorption and scattering maps were generated according to the intensity-based segmentation of the MR images using published optical properties [39]. A reconstruction grid of $28 \times 26 \times 14$ was applied.

Fluorescence reflectance imaging (FRI) was performed for validating the results obtained from FMT experiments. We used the Maestro 500 multi-spectral imaging system (CRi, MA, USA) [40]. Briefly, the imager is equipped with band pass filter (615 to 665 nm) for excitation. The fluorescence signal was detected by a CCD camera mounted on the top of the imaging chamber. Images were acquired by increasing the emission filter central wavelengths by 10-nm increments. For tumor imaging, the field of view comprised the lower abdomen of the mice including the tumor site. Regions of interest (ROIs) at tumor site and skeletal muscle were selected for analysis for both FMT reconstruction results and FRI image.

III. RESULTS

A. Validation of Virtual FMT Function

For each illumination pattern, a mesh was created with 56127 nodes, 327461 tetrahedral elements, and 20756 surface triangular elements (Fig. 4(b)). The positions of detectors (blue squares) and laser sources (red dots) were calculated and attached to the mesh. Excitation and emission procedures were performed with STIFT. For a FMT simulation with $\delta = 1/d$ and $N_{illu} = 8$ in reflection mode, the regularization parameter λ was set to 10^{-4}. After 134 iterations using the CG algorithm convergence was reached with an error tolerance of 10^{-9}. Computational time were: meshing 6.994 s, calculation of excitation field 6.362 s, calculation of emission field 6.290 s, generation of weighting matrix 89.943 s, and solving the inversion problem 27.118 s, resulting in a total time of less than 3 minutes for a complete virtual FMT experiment in reflection mode including forward modelling and inversion. (MATLAB R2012a, MathWorks, US) (Intel Core i7@ 2.60 GHz, RAM 8.00 GB).

The virtual FMT protocol was used to optimize the experimental design during real FMT measurements using #1 with fluorophore inclusion at positions p1 and p2. In the upper panel of Fig. 5, the reconstruction results, at the planes $z = 12$ mm and $y = 15$ mm, are displayed for 4 illumination patterns $\delta = 1/d$ and $N_{illu} = 2, 5, 8, 10$, respectively. The true positions of inclusions are indicated by the dashed lines. For all patterns, the inclusion p1 underneath the center of SF could be resolved. However, due to limited information available for the smallest
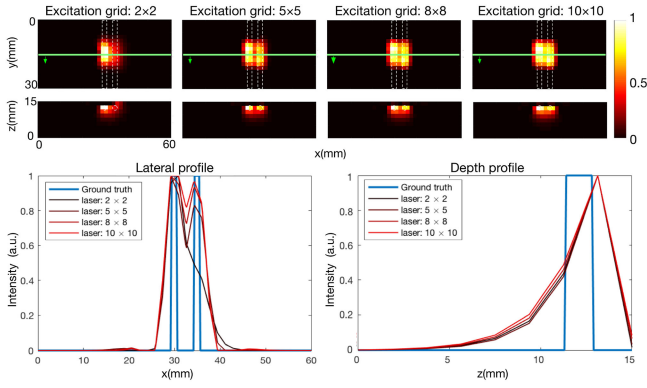
Fig. 5. Validation of virtual FMT protocols. The upper panel shows the reconstructed planes at $z = 12$ mm (3 mm below the top surface) and $y = 15$ mm for four illumination patterns with a fixed illumination density $(1/d)$ and varying numbers of illumination points ($N_{illu} = 2, 5, 8, 10$). The lower left plot shows the lateral profiles (red curves with different levels of darkness) along $y = 15$ mm at plane $z = 12$ mm together with the ground truth (the blue curve), whereas the lower right plot shows the depth profiles along $x = 30$ mm at plane $y = 15$ mm together with the ground truth.
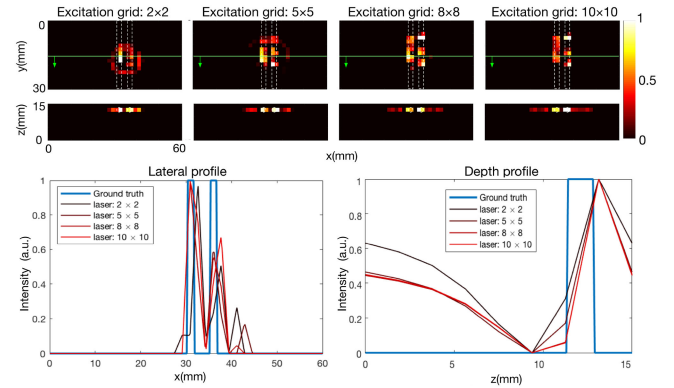

Fig. 7. Validation of real FMT protocols. The upper panel shows the reconstructed planes at $z = 12$ mm (3 mm below the top surface) and $y = 15$ mm for four illumination patterns with a fixed illumination density $(1/d)$ and varying numbers of illumination points $N_{illu} = 2, 5, 8, 10$). The lower left plot shows the lateral profiles (red curves with different levels of darkness) along $y = 15$ mm at plane $z = 12$ mm together with the ground truth (the blue curve), whereas the lower right plot shows the depth profiles along $x = 30$ mm at plane $y = 15$ mm together with the ground truth.
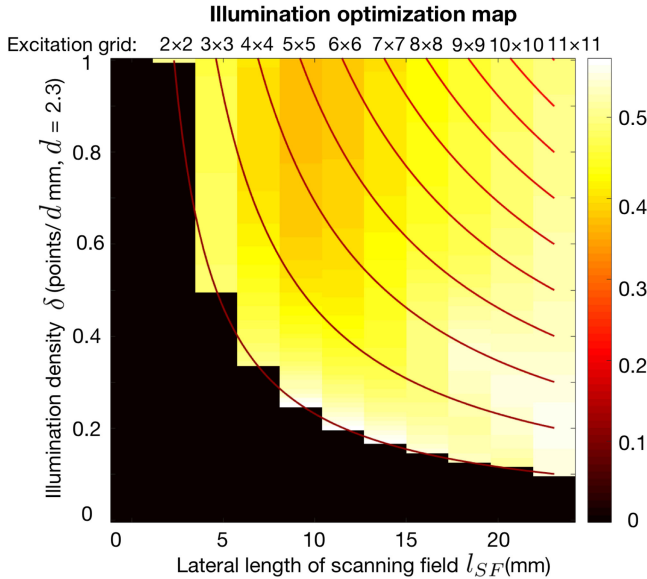

Fig. 6. To find out the optimal illumination pattern, a map of RMSE values with varying illumination densities δ and lateral length of l_{SF} was depicted. The curves indicate different excitation grids with $N_{illu} \times N_{illu}$ laser points. The colorbar indicates the RMSE, darker color indicates smaller RMSE.

2×2 excitation grid covering $SF = 2.3$ mm $\times$ 2.3 mm the signal of the p2 inclusion could not be recovered. Interestingly, the two inclusions located 5 mm apart could be separated better in both lateral and axial planes for the 5×5 ($SF = 11.5$ mm $\times$ 11.5 mm) excitation grid than that from 8×8 ($SF = 18.4$ mm $\times$ 18.4 mm) and 10×10 ($SF = 23$ mm $\times$ 23 mm) grids. This becomes also apparent when analyzing lateral profiles at $y = 15$ mm and $z = 12$ mm, and depth profiles at $y = 15$ mm and $x = 30$ mm (lower panel of Fig. 5).

In order to find the optimal illumination matrix for the actual FMT experiment, we need to consider all meaningful combinations of δ and l_{SF}. For a certain area of SF with $l_{SF} = n\dot{d}$, the number of illumination points increases with $N_{illu} = 2, 3, \ldots, n+1$, and the corresponding illumination density increases with $\delta = 1/nd, 1/(n-1)d, \ldots, 1/d$. For each illumination pattern, the concentration of fluorescent dye was reconstructed and RMSE was used to evaluate the reconstruction quality (Fig. 6). As indicated by the color bar, locations displaying darker yellow values indicate lower RMSE, implying smaller deviations of reconstruction results from the ground truth. Based on this analysis, we conclude that for the specific phantom used $SF = 9.2$ mm $\times$ 9.2 mm and $\delta = 1/2d$ would yield the best reconstruction result. If we assume that at each excitation point the exposure time T_{exp} is fixed, the temporal resolution for a $N_{illu} \times N_{illu}$ excitation grid is $T_{exp} \cdot N_{illu}^2$. Thus the red curves depicted in Fig. 6 represent different temporal resolution. By comparing values of RMSE along those temporal-resolution curves, an optimal combination of illumination density δ and SF covering $l_{SF} \times l_{SF}$ can be recognized, leading to the least error. For example, if we apply a 4×4 excitation grid, a SF covering an area of about 9.2 mm $\times$ 9.2 mm is expected to generate the most robust result.

B. Validation of Experimental FMT Function

1) Validating the Optimization Results From Virtual FMT: Carrying out a virtual FMT protocol allowed testing the feasibility of the FMT experiment defining an optimal illumination pattern for the actual experiment. A series of experiments has therefore been carried out to validate the results of optimization study. Due to the time constraints and in order to simplify experimental design, we fixed the illumination density to $\delta = 1/d$ and varied N_{illu} from 2 to 11. Corresponding to the results obtained from the virtual FMT for $N_{illu} = 2, 5, 8,$ and 10, the reconstruction results at the planes, where $z = 12$ mm (first row) and $y = 15$ mm (second row), were displayed. Similarly, lateral
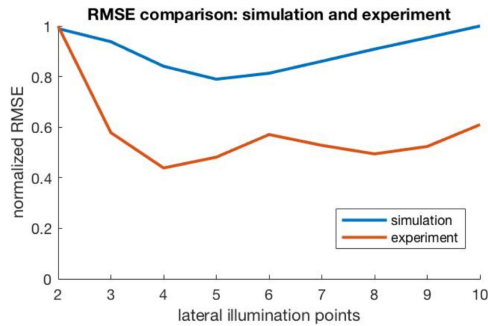
Fig. 8. The illumination density was fixed to $\delta = 1/d$ while N_{illu} changes from 2 to 11. Under this setting, the RMSE values from virtual and experimental FMT protocols were compared to verify the optimization results.
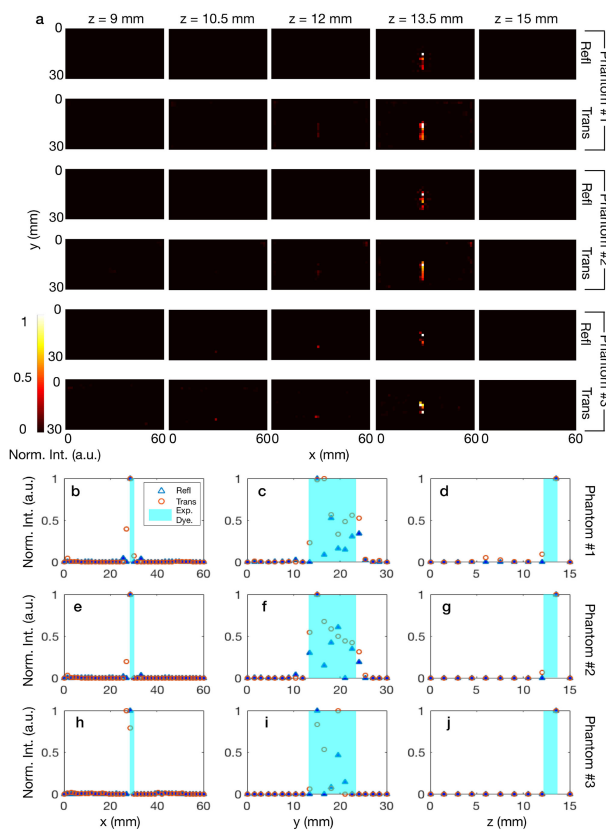
Phantom	1		2		3	
Mode	Refl	Trans	Refl	Trans	Refl	Trans
CNR	39.5	59.6	38.2	56.8	21.9	18.8
RMSE	0.0193	0.0143	0.0192	0.0153	0.0231	0.0249

Normalized RMSE values obtained from the experimental FMT data were compared to those from the virtual experiment to assess the quality of the optimization results. We found good agreement with optimal N_{illu} values of 5 and 4 for virtual and experimental FMT protocols, respectively. Too few or too many illumination points resulted in reconstructed signal that were either blurred or missing features.

2) Extension to More Complicated Objects: We further investigated the performance of STIFT in handling objects of a higher degree of complexity (Fig. 3) using both transmission and reflection mode. Results obtained from the three phantoms for the top five horizontal planes located at 0, 1.5, 3, 4.5 and 6 mm below the top surface (or the highest point of semi-cylindrical phantom) are depicted in Fig. 9(a). Reconstructed profiles along each direction centered at the location (28.5, 15, 13.5) mm are displayed in the lower panel of in Fig. 9. Both reconstructed planes and profiles demonstrate that the position of the fluorescent inclusion can be accurately resolved in a good agreement with the expected dye distribution (light blue area in Fig. 9(b-j)). Both lateral and depth resolution reaches about 1.5 mm in all three phantoms with both reflection and transmission modes. CNR and RMSE values in in Table II reveal the reconstruction quality more quantitatively. Regardless of measurement modes, STIFT achieves almost twice higher CNR and 30% lower RMSE in slab phantoms #1 and #2 than in the semi-cylindrical phantom #3. For different measurement modes, transmission mode generally enables higher CNR and lower RMSE than reflection mode. This difference of CNR and RMSE is significant for phantom #1 and #2, but less obvious for phantom #3.

3) In Vivo Application With a Tumor Animal Model: A mesh containing 3092 nodes, 17730 tetrahedral elements and 1204 surface elements was generated from the T2*-weighted MR image (Fig. 10(a)). Transverse, sagittal and coronal planes of the combined MRI/FMT data set is shown for the intersection point located at the tumor (Fig. 10(b)). High FMT values were observed at the tumor site, mainly at the interface to the skeletal muscle tissue. Bright signals were also seen at the peripheral tissue near the tumor site, which might be accumulation of the ProSense. The in vivo fluorescent image shows the lower body of the mouse (Fig. 10(c)), revealing high concentration of activated ProSense in the tumor and to a less degree at the skeletal muscle tissue on the left flank (Fig. 10(d)).

Fig. 9. The upper panel (a) shows five reconstructed planes ($z = 9$, 10.5, 12, 13.5, 15 mm) for three phantoms with reflection and transmission modes. Odd rows indicate reflection, even rows transmission mode for the respective phantoms with $z = 15$ mm indicating the top surface of each phantom. The lower panel (b–j) shows reconstructed profiles along x-, y- and z- axes centered at the location (28.5, 15, 13.5) mm for each phantom. Profiles achieved from reflection mode (blue lines) and transmission mode (red lines) are compared to the expected distribution of fluorescent dye (light blue area). (Refl: reflection mode; Trans: transmission mode; Exp. Dye: expected distribution of fluorescent dye; Norm. Int.: normalized reconstructed intensity.)

profiles at $y = 15$ mm and $z = 12$ mm, and depth profiles at $y = 15$ mm and $x = 30$ mm are shown. We found similar results as the virtual FMT, the 2×2 excitation grid with limited area of scanning was not able to resolve two inclusions while the other three patterns could separate both capillaries.

IV. DISCUSSION

A. Features of STIFT

The software package STIFT was designed to facilitate FMT experiments by bridging the gaps between simulation, actual experiments, and data reconstruction. The ultimate goal was
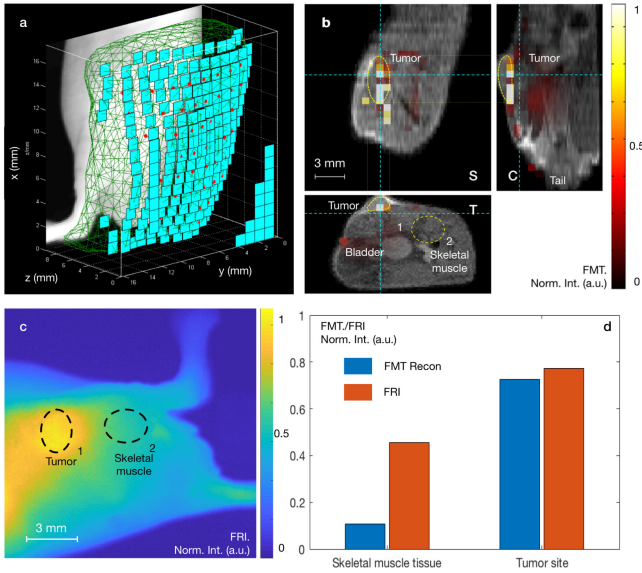
Fig. 10.   MRI derived structural information was used for reconstructing the object in 3D and adaptive meshing was performed (a), with detector elements (green patch) and laser illumination points (red spots) assigned to the surface of the mesh. FMT reconstruction shows the distribution of protease-activated ProSense in mouses lower abdomen (b), with transverse (T), coronal (C) and sagittal (S) planes intersecting at the tumor site on the left flank. (c) *In vivo* fluorescent planar image with the same mouse shows high intensity on the tumor site, in a good agreement with FMT result. Mean values of two ROIs at tumor site (#1) and skeletal muscle (#2) are calculated for both FMT and FRI images (d).

to provide a tool that assists non-expert users in the proper choice of experimental settings and ensures the accuracy of reconstruction algorithm. The workflow of STIFT can be largely controlled by the user. We suggest three basic protocols for any FMT experiment: virtual FMT simulation/reconstruction, FMT experiment/data collection, and tomographic reconstruction of experimental data. Features incorporated in STIFT are 1) self-adaptive meshing: the accuracy of FEM solution depends largely on the quality of the mesh. A mesh with very fine elements is a commonly known method to improve the quality of the results, but also demands for long computation time. Here, we implemented a seamless protocol plugging voxelized datasets, such as MRI structural images or assumed segmented data, into an optimized tetrahedral mesh. Geometry-adaptive refinement is used to treat the edges in the structure, while illumination-adaptive refinement corrects the high relative error close to the laser sources. Hence, even for the same object, the mesh will be adapted upon changing the illumination pattern. This refinement typically increases the node number by only 10–20%, but it signifcantly improves the mesh quality. 2) Image registration: we implemented a landmark-based registration function, which guarantees the processing of optical data and structural reference data (e.g., derived from MRI) the same coordinate system. In a multimodal system combining fluorescent readouts with CT or MRI data, image registration is an inevitable process for both reconstruction and final analysis. Thus additional codes dealing with data fusion will be required. Although the commonly used DOT toolbox NIRFast, provides other alternative

software tools to perform registration, STIFT does not require external software or data transfer. 3) Mapping technique: some FMT reconstruction algorithms aim at solving for the unknown variable at each node, which is a straightforward but not very practical approach. Too many unknowns require extremely long computational time and render the solutions unstable. Adaptive meshing or multi-mesh methods have been previously reported [12]. However, adaptive meshing should be applied not only to the unknown but also to other data domains such as optical property maps and detector planes. Thus, we simplified the problem by introducing only one optimal designed mesh, which guarantees accuracy in forward modelling. The reconstruction quality is controlled by the dimension of the grid storing the reconstruction results and multiple trials of different dimensions are feasible. 4) The output data is formatted as the STIFT class, which not only contains the reconstruction results but also traces the history of the entire FMT experiments. This is important for future comparison with other FMT studies.

B. Optimization and Reconstruction

Taking advantage of the integrative property of STIFT, multiple loops of virtual FMT protocols can be performed first to evaluate the feasibility and define an optimal experimental setting, basically optimizing the illumination pattern. A slab phantom with two capillaries was used to illustrate this function. The reconstruction quality was determined by computing RMSE values with regard to the known ground truth. We also introduced a RMSE map with the horizontal axis indicating the lateral length of SF and the vertical one the illumination density (Fig. 6). Recording too few illumination points will render the weighting matrix low ranked, thus leading to a wrong reconstruction result. On the other hand, a high number of illumination points will add irrelevant information (noise), thereby degrading the quality of the reconstruction. However, the experimental results indicate that for a fixed δ, RSME values are rather insensitive towards increasing N_{illu}, i.e., the size of SF will not affect the result too much as long as it is larger than the optimal value. Apart from the requirement that the SF should be at least as large as the inclusion, we have to also ensure that the sampling frequency is sufficient to capture the internal structure of the inclusion. As a rule of thumb we may formulate that

a) the SF should be at least twice the dimension of the region of interest, i.e., for the phantoms described twice the separation of the inclusions ($2d_{sep}$), and

b) the sampling distance, i.e., distance between two source points should be smaller than half the characteristic distance of the internal structure, i.e., $d_{sep}/2$ in our case.

While this rule of thumb holds reasonably well for reflection mode CW-FMT in order to recover signals from sources located at a depth of a few millimeters, it is unclear whether it can be generalized. In addition, RMSE is not the only index to determine the quality of reconstruction. Alternatively reconstruction quality could be evaluated by singular value analysis (SVA) of the weighting matrix. SVA has been applied in optimizing the FMT configuration, which includes the source/detector arrangement [16], the field-of-view [15], [16], the transmission/emission

selection [15], or the 360-degree-projection mode [4]. Irrespective of the quality assessment used, we are convinced that the option of carrying virtual FMT experiments provided by STIFT will improve the actual experiments both with regard to efficiency and accuracy.

The reconstruction module of STIFT allowed resolving Cy5.5 inclusions accurately and reliably without creating obvious artefacts for three phantoms of increasing complexity for both reflection- and transmission-mode FMT operation. Generally, transmission mode yields better reconstruction than reflection mode with lower RMSE and higher CNR, which has been demonstrated with both homogeneous and heterogeneous slab phantoms (but less evident with the semi-cylindrical phantom). This finding corresponds well with the previously reported result using SVA [5].

Following the phantom-based validation, we have successfully applied STIFT in a proof-of-concept task of imaging a tumor model. Measurement data was mapped into the computational model through landmark-based registration between the topological MRI map and the white-light image (Supple. Fig. 6d). STIFT is also capable of meshing a complex object with an irregular surface like a real mouse (Fig. 10(b)). From the FMT reconstruction result, we observed high ProSense deposit in the subcutaneous tumor and its peripheral tissues. Little uptake was found in the skeletal muscle tissue, which agrees well with the results shown in FRI method.

C. Limitations of STIFT

Nevertheless, STIFT in its current format is subject to several limitations. i) The forward modelling kernel of STIFT is the DE, which is solved in the context of an FEM approach. The DE is an approximation of the more general radiation transfer equation that holds true for a strongly scattering medium, in which photon propagation becomes undirected due to multiple scatterings [2], [6]. The collapse of the DE in low- or non-scattering area such as cerebrospinal fluid is commonly known. Similarly, the DE breaks down for structures close to the surface (within a few scattering lengths). To tackle the problem, a more sophisticated forward model like MC-based methods should be applied, which is however highly resource intense. The issue regarding computation time, which is considered a major drawback of all MC-based methods, could be remedied with parallel computing using large-scale clusters or general purposed graphics processing units (GP-GPU) [26]. Further improvement in computational speed can be achieved by adopting the concept of a tetrahedral mesh instead of a voxelized grid [27], [41], [42]. Due to the modular nature of STIFT, any advanced forward model might be integrated in a rather straightforward manner. ii) The registration method currently implemented in STIFT is based on operator-interactive landmark selection. Although artificial fiducial points can be selected in addition to natural landmarks, registration results will depend on the skills of the operator. The current version of image registration uses three pairs of landmark points. Use of more points in combination with a least square algorithm will help to reduce the statistical errors from the operator interaction. Again the modular nature of STIFT

allows implementation of alternative registration procedures. iii) STIFT aims at reducing operation during the FMT experimental pipeline. In the current version, the number and positions of laser points can still be selected by the user and the evaluation of both simulation and experimental results is subjective. In future, we plan to implement full automation of the virtual FMT module. As a result, the illumination pattern will be determined automatically. User interaction will be facilitated by a GUI. iv) Currently, STIFT is designed to facilitate the most basic version of CW-mode FMT, with fixed camera position, and operation in both transmission and reflection modes. From a hardware point of view, this is not difficult, as laser generators, filters, and cameras are all available at reasonable price. Obviously, the use of STIFT is not limited to the standalone FMT, but can also be extended to hybrid systems. As we left the controlling module open, and any hardware driver could be integrated.

V. CONCLUSION

We have described STIFT, a comprehensive software platform based on FEM for simulation, reconstruction, and validation of FMT experiments. STIFT comprises three major protocols: virtual FMT, control of actual FMT measurements, and reconstruction of experimental FMT data. Features of STIFT are self-adaptive meshing, image registration, free-space detection, and mapping techniques between meshes and grids. Phantom validation demonstrated that the software can be used for optimization of FMT experiments, in particular for optimizing illumination patterns. Robust reconstruction results have been obtained both for homogeneous and heterogeneous tissue mimicking phantoms containing fluorescent inclusions. Advanced forward models and the development of a GUI will further enhance the performance and user-friendliness of STIFT.

REFERENCES

[1] R. Weissleder and V. Ntziachristos, "Shedding light onto live molecular targets," *Nat. Med.*, vol. 9, no. 1, pp. 123–128, 2003. [Online]. Available: https://www.ncbi.nlm.nih.gov/pubmed/12514725

[2] F. Stuker, J. Ripoll, and M. Rudin, "Fluorescence molecular tomography: Principles and potential for pharmaceutical research," *Pharmaceutics*, vol. 3, no. 2, pp. 229–74, 2011. [Online]. Available: https://www.ncbi.nlm.nih.gov/pubmed/24310495

[3] C. Darne, Y. J. Lu, and E. M. Sevick-Muraca, "Small animal fluorescence and bioluminescence tomography: A review of approaches, algorithms and technology update," *Phys. Med. Biol.*, vol. 59, no. 1, pp. R1–R64, 2014.

[4] T. Lasser and V. Ntziachristos, "Optimization of 360 degrees projection fluorescence molecular tomography," *Med. Image Anal.*, vol. 11, no. 4, pp. 389–399, 2007.

[5] J. Culver *et al.*, "Optimization of optode arrangements for diffuse optical tomography: A singular-value analysis," *Opt. Lett.*, vol. 26, no. 10, pp. 701–703, 2001.

[6] F. Stuker, "Hybrid imaging: Combining fluorescence molecular tomography with magnetic resonance imaging," Ph.D. dissertation, ITET, Zürich, Switzerland, 2011.

[7] Q. Pian *et al.*, "Hyperspectral time-resolved wide-field fluorescence molecular tomography based on structured light and single-pixel detection," *Opt. Lett.*, vol. 40, no. 3, pp. 431–434, 2015.

[8] H. B. Jiang, "Frequency-domain fluorescent diffusion tomography: A finite-element-based algorithm and simulations," *Appl. Opt.*, vol. 37, no. 22, pp. 5337–5343, 1998.

[9] V. Ntziachristos, C. Bremer, and R. Weissleder, "Fluorescence imaging with near-infrared light: New technological advances that enable in vivo molecular imaging," *Eur. Radiol.*, vol. 13, no. 1, pp. 195–208, 2003.

[10] S. Zhang *et al.*, "Robust reconstruction of fluorescence molecular tomography based on sparsity adaptive correntropy matching pursuit method for stem cell distribution," *IEEE Trans. Med. Imag.*, vol. 37, no. 10, pp. 2176–2184, Oct. 2018.

[11] X. Zhang, J. Zhang, and J. Luo, "Reconstruction of in vivo fluorophore concentration variation with structural priors and smooth penalty," *Appl. Opt.*, vol. 55, no. 10, pp. 2732–2740, 2016.

[12] X. L. Song *et al.*, "Reconstruction for free-space fluorescence tomography using a novel hybrid adaptive finite element algorithm," *Opt. Exp.*, vol. 15, no. 26, pp. 18300–18317, 2007.

[13] G. Quan *et al.*, "Monte carlo-based fluorescence molecular tomography reconstruction method accelerated by a cluster of graphic processing units," *J. Biomed. Opt.*, vol. 16, no. 2, 2011, Art. no. 026018.

[14] A. X. Cong and G. Wang, "A finite-element-based reconstruction method for 3d fluorescence tomography," *Opt. Exp.*, vol. 13, no. 24, pp. 9847–9857, 2005.

[15] J. Dutta *et al.*, "Illumination pattern optimization for fluorescence tomography: Theory and simulation studies," *Phys. Med. Biol.*, vol. 55, no. 10, pp. 2961–2982, 2010.

[16] E. E. Graves *et al.*, "Singular-value analysis and optimization of experimental parameters in fluorescence molecular tomography," *J. Opt. Soc. Amer. A, Opt. Image Sci., Vis.*, vol. 21, no. 2, pp. 231–241, 2004.

[17] J. Dutta, "Computational methods for fluorescence molecular tomography," Ph.D. dissertation, Viterbi School Eng., Univ. Southern California, Los Angeles, CA, USA, 2011.

[18] M. Schweiger and S. Arridge, "The toast++ software suite for forward and inverse modeling in optical tomography," *J. Biomed. Opt.*, vol. 19, no. 4, 2014, Art. no. 040801.

[19] H. Dehghani *et al.*, "Near infrared optical tomography using nirfast: Algorithm for numerical model and image reconstruction," *Commun. Numer. Methods Eng.*, vol. 25, no. 6, pp. 711–732, 2008.

[20] M. Jermyn *et al.*, "Fast segmentation and high-quality three-dimensional volume mesh creation from medical images for diffuse optical tomography," *J. Biomed. Opt.*, vol. 18, no. 8, 2013, Art. no. 86007.

[21] "3d slicer website," Accessed: Jan. 30, 2018. [Online]. Available: https://www.slicer.org

[22] "Simulation based approach to fluorescence diffuse optical tomography," Accessed: Jan. 30, 2018. [Online]. Available: https://www.comsol.eu/paper/simulation-based-approach-to-fluorescence-d\%iffuse-optical-tomography-10345

[23] C. Geuzaine and J.-F. Remacle, "GMSH: A 3-d finite element mesh generator with built-in pre-and post-processing facilities," *Int. J. Numer. Methods Eng.*, vol. 79, no. 11, pp. 1309–1331, 2009.

[24] P. C. Hansen and M. Saxild-Hansen, "Air tools-a MATLAB package of algebraic iterative reconstruction methods," *J. Comput. Appl. Math.*, vol. 236, no. 8, pp. 2167–2178, 2012.

[25] L. V. Wang and H. I. Wu, *Biomedical Optics: Principles and Imaging*. Hoboken, NJ, USA: Wiley, 2007.

[26] Q. Q. Fang and D. A. Boas, "Monte carlo simulation of photon migration in 3d turbid media accelerated by graphics processing units," *Opt. Exp.*, vol. 17, no. 22, pp. 20178–20190, 2009.

[27] Q. Q. Fang, "Mesh-based monte carlo method using fast ray-tracing in plucker coordinates," *Biomed. Opt. Exp.*, vol. 1, no. 1, pp. 165–175, 2010.

[28] R. B. Schulz, J. Ripoll, and V. Ntziachristos, "Noncontact optical tomography of turbid media," *Opt. Lett.*, vol. 28, no. 18, pp. 1701–1703, 2003.

[29] V. Ntziachristos and R. Weissleder, "Experimental three-dimensional fluorescence reconstruction of diffuse media by use of a normalized born approximation," *Opt. Lett.*, vol. 26, no. 12, pp. 893–895, 2001.

[30] A. D. Klose, V. Ntziachristos, and A. H. Hielscher, "The inverse source problem based on the radiative transfer equation in optical molecular imaging," *J. Comput. Phys.*, vol. 202, no. 1, pp. 323–345, 2005.

[31] R. H. Byrd *et al.*, "A limited memory algorithm for bound constrained optimization," *SIAM J. Scientific Comput.*, vol. 16, no. 5, pp. 1190–1208, 1995.

[32] Q. Q. Fang and D. A. Boas, "Tetrahedral mesh generation from volumetric binary and gray-scale images," in *Proc. IEEE Int. Symp. Biomed. Imag., Nano Macro*, vol. 1/2, 2009, pp. 1142–1145.

[33] J. Ripoll, R. B. Schulz, and V. Ntziachristos, "Free-space propagation of diffuse light: Theory and experiments," *Phys. Rev. Lett.*, vol. 91, no. 10, 2003, Art. no. 103901.

[34] X. Zhang *et al.*, "Fast reconstruction of fluorophore concentration variation based on the derivation of the diffusion equation," *J. Opt. Soc. Amer. A, Opt. Image Sci., Vis.*, vol. 32, no. 11, pp. 1993–2001, 2015.

[35] J.-C. Baritaux, K. Hassler, and M. Unser, "An efficient numerical method for general lp regularization in fluorescence molecular tomography," *IEEE Trans. Med. Imag.*, vol. 29, no. 4, pp. 1075–1087, Apr. 2010.

[36] W. Ren *et al.*, "Dynamic measurement of tumor vascular permeability and perfusion using a hybrid system for simultaneous magnetic resonance and fluorescence imaging," *Mol. Imag. Biol.*, vol. 18, no. 2, pp. 191–200, 2016.

[37] R. Weissleder *et al.*, "In vivo imaging of tumors with protease-activated near-infrared fluorescent probes," *Nature Biotechnol.*, vol. 17, no. 4, pp. 375–378, 1999.

[38] "Data sheet for prosense 680 fluorescent imaging agent," Accessed: Feb. 20, 2019. [Online]. Available: http://www.perkinelmer.com/product/prosense-680-nev10003

[39] S. L. Jacques, "Optical properties of biological tissues: A review," *Phys. Med. Biol.*, vol. 58, no. 11, pp. R37–R61, 2013.

[40] J. Klohs *et al.*, "In vivo near-infrared fluorescence imaging of matrix metalloproteinase activity after cerebral ischemia," *J. Cerebral Blood Flow Metabolism*, vol. 29, no. 7, pp. 1284–1292, 2009.

[41] H. Shen and G. Wang, "A tetrahedron-based inhomogeneous monte carlo optical simulator," *Phys. Med. Biol.*, vol. 55, no. 4, pp. 947–962, 2010.

[42] H. Li *et al.*, "A mouse optical simulation environment (MOSE) to investigate bioluminescent phenomena in the living mouse with the monte carlo method," *Academic Radiol.*, vol. 11, no. 9, pp. 1029–1038, 2004.